## Anderson impurity solver integrating tensor network methods with quantum computing

François Jamet, <sup>1,\*</sup> Connor Lenihan, <sup>1</sup> Lachlan P. Lindoy, <sup>1</sup> Abhishek Agarwal, <sup>1</sup> Enrico Fontana, <sup>1,2</sup> Baptiste Anselme Martin, <sup>3,4</sup> and Ivan Rungger<sup>1,†</sup>

<sup>1</sup> National Physical Laboratory, Teddington, TW11 0LW, United Kingdom

<sup>2</sup> Department of Computer and Information Sciences, University of Strathclyde,

26 Richmond Street, Glasgow G1 1XH, United Kingdom

<sup>3</sup> TotalEnergies, Tour Coupole - 2 place Jean Millier 92078 Paris la Défense, France

<sup>4</sup> Universite Paris-Saclay, CNRS, Laboratoire de Physique des Solides, 91405, Orsay, France

Solving the Anderson impurity model typically involves a two-step process, where one first calculates the ground state of the Hamiltonian, and then computes its dynamical properties to obtain the Green's function. Here we propose a hybrid classical/quantum algorithm where the first step is performed using a classical computer to obtain the tensor network ground state as well as its quantum circuit representation, and the second step is executed on the quantum computer to obtain the Green's function. Our algorithm exploits the efficiency of tensor networks for preparing ground states on classical computers, and takes advantage of quantum processors for the evaluation of the time evolution, which can become intractable on classical computers. We demonstrate the algorithm using 20 qubits on a quantum computing emulator for SrVO<sub>3</sub> with a multi-orbital Anderson impurity model within the dynamical mean field theory. The tensor network based ground state quantum circuit preparation algorithm can also be performed for up to 40 qubits with our available computing resources, while the state vector emulation of the quantum algorithm for time evolution is beyond what is accessible with such resources. We show that, provided the tensor network calculation is able to accurately obtain the ground state energy, this scheme does not require a perfect reproduction of the ground state wave function on the quantum circuit to give an accurate Green's function. This hybrid approach may lead to quantum advantage in materials simulations where the ground state can be computed classically, but where the dynamical properties cannot.

The simulation of strongly correlated quantum systems is one of the most promising applications of quantum computers [1, 2]. This is due to the potential for quantum processors to perform computations using exponentially fewer resources than classical computers for such systems. The most widely used classical computing method for simulations of real materials with strongly correlated electrons is based on the dynamical mean field theory (DMFT), which self-consistently maps the periodic Hubbard model onto an effective Anderson impurity model (AIM) containing only a few interacting impurity sites embedded in a non-interacting bath [3–6]. Despite the development of a large number of impurity solvers over the years [7–17], none of them have achieved universal applicability. Therefore, the solution of the AIM remains a challenging problem for classical computers, where a quantum computer may have an advantage. Hybrid quantum-classical approaches are the most promising way to achieve such advantage, where only those parts of the algorithm which are the most challenging for a classical computer, are executed on a quantum computer [18, 19]. One successful class of classical computing impurity solvers includes algorithms which make use of tensor network (TN) methods [8–13], which are efficient in obtaining the ground state (GS) and also the first few excited states of the system. However, the time evolution

of complex impurity models required as part of the AIM solver remains a challenge due to the rapid growth of the bond dimension with time, making long-time calculations unfeasible [20, 21].

In this article we propose an approach that combines classical and quantum computing resources to address the problem of multi-orbital AIMs. The proposed algorithm entails obtaining the GS of the multi-orbital AIM using a TN representation of the wave function [8, 9, 22] on a conventional processor, and subsequently a quantum circuit is constructed to represent this wave function. The form of this quantum circuit is also constructed using a conventional processor. Finally, one uses a quantum computer to simulate the time evolution of the prepared initial quantum states. In doing so, we are able to compute dynamical observables such as the Green's function (GF), a central mathematical object in materials calculations. Several physical observables can be computed from the GF, such as the density of states (DOS) [23]. This algorithm has the potential to surpass existing impurity solvers in situations where TN-based techniques can compute the GS, but where the growth in entanglement entropy observed during the course of time evolution [9], and the subsequent increase in bond dimension [12], limits the timescale over which dynamics can be obtained [13].

<sup>\*</sup> francois.jamet@francoisjamet.fr

<sup>†</sup> ivan.rungger@npl.co.uk

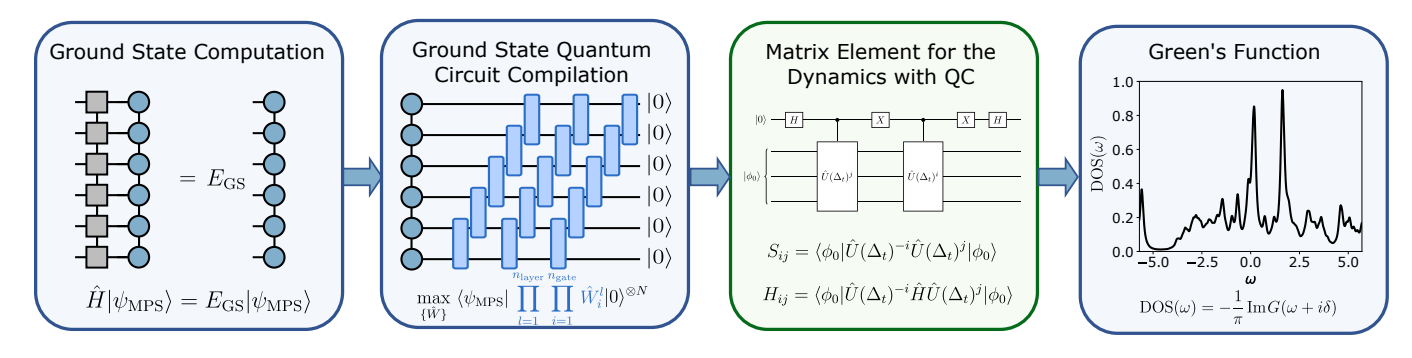


Figure 1. Schematic of the combined classical/quantum algorithm for computing the Green's function of the Anderson impurity model. Blue panels indicate the parts of the algorithm that are run on the classical computer, while the green panel indicates the steps to be executed on a quantum computer. The algorithm consists of four sequential steps (shown as separate panels): 1. the computation of the ground state energy and MPS representation of the wave function using the DMRG algorithm (classical); 2. the construction of a parametric quantum circuit representation of this wave function (classical); 3. the simulation of the dynamics by evaluation of the matrix elements through time evolution (quantum); 4. the evaluation of a continued fraction expansion of the Green's function using the computed matrix elements (classical).

The Hamiltonian of the AIM is given by [3, 4]

$$H = \sum_{ij}^{n_{\text{imp}}} \sum_{\sigma} \epsilon_{ij} \hat{c}_{i\sigma}^{\dagger} \hat{c}_{j\sigma} + \sum_{ijkl}^{n_{\text{imp}}} \sum_{\sigma\sigma'} U_{ijlk} \hat{c}_{i\sigma}^{\dagger} \hat{c}_{j\sigma'}^{\dagger} \hat{c}_{k\sigma'} \hat{c}_{l\sigma}$$
$$+ \sum_{i}^{n_{\text{imp}}} \sum_{j}^{n_{b}} \sum_{\sigma} V_{ij} (\hat{c}_{i\sigma}^{\dagger} \hat{d}_{j\sigma} + \hat{d}_{j\sigma}^{\dagger} \hat{c}_{i\sigma}) + \sum_{\sigma} \sum_{ij}^{n_{b}} \epsilon_{ij}^{d} \hat{d}_{i\sigma}^{\dagger} \hat{d}_{j\sigma} ,$$

$$(1)$$

where  $\hat{c}_{i\sigma}^{\dagger}$ ,  $\hat{c}_{i\sigma}$  ( $\hat{d}_{i\sigma}^{\dagger}$ ,  $\hat{d}_{i\sigma}$ ) are the creation and annihilation operators of an electron of spin  $\sigma$  on the *i*-th impurity site (bath site);  $\epsilon_{ij}$  and  $U_{ijlk}$  are the hopping and interacting matrices between the impurity orbitals,  $\epsilon_{ij}^d$  is the hopping matrix between the bath orbitals, and  $V_{ij}$  is the hybridization matrix between impurity orbitals and bath orbitals. Differently from a general chemistry Hamiltonian, the interaction term in the AIM is confined to the impurity sites, thereby considerably reducing the number of terms in the Hamiltonian, which is proportional to  $n_{\rm imp}^4 + (n_{\rm imp} + n_{\rm bath})^2$ , where  $n_{\rm imp}$  ( $n_{\rm bath}$ ) is the number of impurity sites (bath sites).

The zero temperature greater and lesser GFs are defined as

$$G_{\alpha\beta}^{>}(z) = \langle \text{GS} | \hat{c}_{\alpha}(z - (\hat{H} - E_{\text{GS}}))^{-1} \hat{c}_{\beta}^{\dagger} | \text{GS} \rangle,$$
 (2)

$$G_{\alpha\beta}^{<}(z) = \langle \text{GS} | \hat{c}_{\alpha}^{\dagger}(z + (\hat{H} - E_{\text{GS}}))^{-1} \hat{c}_{\beta} | \text{GS} \rangle, \qquad (3)$$

respectively, where  $|\mathrm{GS}\rangle$  is the GS wave function,  $E_{\mathrm{GS}}$  the GS energy, and  $\alpha$  indexes both spin and site indices. These GFs can be used to obtain the retarded GF as  $G_{\alpha\beta}(z) = G_{\alpha\beta}^{>}(z) + G_{\alpha\beta}^{<}(z)$ . In what follows we consider only the diagonal elements of the GFs, so that  $\beta=\alpha$ , and for ease of notation we discard the orbital index subscript, in analogy to the approach in Ref. [24], where the extension to the off-diagonal elements is also presented. The imaginary part of the retarded GF gives the density of states (DOS),  $\mathrm{DOS}(\omega) = -\frac{1}{\pi}\mathrm{Im}G(\omega+i\delta)$ , for  $\omega$  a real energy, and  $\delta$  a small positive number. For the AIM

DOS only the impurity orbitals GFs need to be computed, which significantly reduces the number of terms compared to more general models, reducing the needed computational resources.

The first step of our algorithm, schematically illustrated in the left-most panel in Fig. 1, is the computation of the GS wave function and energy using a TN representation. Here we use a matrix product state (MPS) representation. We note that this algorithm can be extended to other TN forms, such as tree tensor networks [9] and fork tensor networks [8], which have been successfully used in the context of quantum impurity models. The MPS GS wave function of a quantum impurity model, which we denote by  $|\psi_{\rm MPS}\rangle$ , can be obtained with the density matrix renormalization group (DMRG) method [25–28]. We make use of the ITensor Library [29, 30] for the MPS calculations.

Once the GS is obtained with the MPS representation, we use the method proposed in Ref. [31], and improved in Ref. [32], to construct a quantum circuit representing the GS wave function, which we denote as  $|\psi_{\rm OC}\rangle$ . Ref. [31] introduces a protocol for a fixed number of layers with a staircase topology composed of two-qubit gates, and Ref. [32] proposes a method for iteratively adding layers of staircases to this protocol. Similar strategies have been proposed in Refs. [33] and [34]. In this article we extend this approach to include  $n_{\rm g}$ -qubit gates, where  $n_{\rm g} > 1$ is the number of qubits on which the gate acts. When represented as a matrix, an  $n_{\rm g}$ -qubit gate corresponds to a  $2^{n_g} \times 2^{n_g}$  unitary matrix. Such general  $n_g$ -qubit gates can be expanded in a sequence of 2-qubit gates combined with single qubit rotations using the Shannon decomposition [35]. The circuit depth and with it the number of CNOT gates of such a decomposition increases significantly for increasing  $n_g$  (see Appendix A).

The approach involves applying a series of staircase layers of  $n_{\rm g}$ -qubit gates, with  $n_{\rm g} \leq \lceil \log_2{(\chi_{\rm max})} \rceil + 1$ , where  $\chi_{\rm max}$  is the maximum bond dimension of the tar-

geted TN [36]. These gates are applied on an initial state that is easy to prepare on a quantum computer, usually  $|0\rangle^{\otimes N}$ , where N is the total number of qubits required to represent the state, so that the quantum circuit representation of the wave function may be written as  $|\psi_{\rm QC}\rangle = \prod_{l=1}^{n_{\rm layer}} \prod_{i=1}^{n_{\rm gate}} \hat{W}^l_i |0\rangle^{\otimes N}$ . Here,  $n_{\rm layer}$  is the number of staircase layers,  $n_{\rm gate} = N+1-n_g$  is the number of  $n_{\rm g}$ -qubit gates per layer, and  $\hat{W}^l_i$  denotes the i-th  $n_{\rm g}$ -qubit gate in layer l. The quantum circuit is schematically illustrated with the blue-colored layers of gates in the second panel in Fig. 1. The choice of  $n_{\rm g}$  and  $n_{\rm layer}$  in the circuit ansatz depends on the required accuracy of the solution.

This parametric circuit is optimized on a classical computer by maximising the absolute value of the overlap, f, between the trial quantum state,  $|\psi_{\rm QC}\rangle$ , and the MPS GS wave function,  $|\psi_{\rm MPS}\rangle$ :

$$f[\{\hat{W}\}] = |\langle \psi_{\text{MPS}} | \psi_{\text{QC}} \rangle|. \tag{4}$$

We construct this optimized parametric circuit by progressively increasing the number of layers,  $n_{\text{layer}}$ , of  $n_{\text{g}}$ qubit gates included in the circuit. At each stage we sequentially update each  $n_{\rm g}$ -qubit gate,  $\hat{W}_i^l$ , to locally maximise the overlap with the MPS GS. We optimise each  $\hat{W}_{i}^{l}$  in order of increasing i within a given layer, l, before proceeding to optimise each gate in the next layer. This sweeping process is repeated until the improvement made to the overlap with the target MPS state through a sweep falls below a set tolerance, at which point an additional staircase layer of  $n_{\rm g}$ -qubit gates is added. When adding a new staircase layer we initialise all gates in the new layer as the identity operator. We explored the use of alternative initialisation strategies that make use of low bond dimension approximations to the MPS wavefunction [32]. However, for the ground state wavefunctions considered here, we observed significant growth in the bond dimension of the MPSs used throughout the optimisation process when using this alternative initialization, limiting the depth of circuit for which optimization was practical.

For each of the sequential updates used in this optimization scheme, the  $n_{\rm g}$ -qubit operator  $\hat{O}_i^l$  that optimizes the loss function can be found analytically [32, 33]. In general,  $\hat{O}_i^l$  is not unitary. The  $n_{\rm g}$ -qubit unitary that minimises f can therefore be obtained by finding the unitary that closest approximates  $\hat{O}_i^l$ . This can be done using a singular value decomposition of  $\hat{O}_i^l = U^{\dagger}SV$ , giving the closest unitary as  $U^{\dagger}V$  [31–33, 37, 38]. Following Ref. [32], we employ MPS representations of the intermediate states required to evaluate  $\hat{O}_i^l$  in order to allow for efficient classical optimization of the quantum circuit. The order of optimization used here allows to reuse the intermediate states constructed when optimizing individual tensors [32], which significantly improves the efficiency of the algorithm. The optimization process is schematically illustrated in the second panel in Fig. 1. We note here that one does not use a quantum computer

to perform the minimization, and that all these computations are performed using MPS representations of the quantum states.

The quantum circuit optimized on the classical computer can now be executed on a quantum computer, so that  $|\psi_{\rm QC}\rangle$  is produced on the quantum computer. We use it as starting point to perform its time evolution on the quantum computer and with it obtain the GF. There are several quantum algorithms that use the time evolution of quantum states to compute the GF on a quantum computer [18, 24, 39-47], which differ in scalability and required quantum resources. Here, we use a modified version of the quantum subspace expansion algorithm for GFs (QSEG) [24] due to its potential scalability to large systems with a moderate number of required Trotter steps. Compared to the QSEG algorithm in Ref. [24], here we obtain the GS wave function directly on the quantum computer using the MPS based circuit outlined above. This significantly reduces the number of matrix elements that need to be evaluated on a quantum computer when compared to Ref. [24].

Within QSEG the greater GF in Eq. 2 is represented using a Krylov basis set with a continued fraction

$$G^{>}(z) = \frac{1}{z - a_0 - \frac{b_1^2}{z - a_1 - \frac{b_2^2}{z - a_2}}},$$
 (5)

and analogously for the lesser GF. The  $a_i$  and  $b_i$  are obtained using the Lanczos algorithm, which orthogonalizes the Krylov basis, defined as  $|\phi_0\rangle$ ,  $H|\phi_0\rangle$ ,  $H^2|\phi_0\rangle$ ..., where  $|\phi_0\rangle = \hat{c}^{\dagger}|\text{GS}\rangle$ . Since the creation operator is a sum of two Pauli strings, the state  $|\phi_0\rangle$  is also a sum of two wave vectors, one for each of these Pauli strings [24]. Once orthogonalized within the Lanczos scheme, the Hamiltonian is tridiagonal in this basis, bringing the GF in Eq. 2 into the continued fraction representation presented in the equation above.

To represent the Krylov basis we use the QSEG framework of Ref. [24], where each Krylov vector is decomposed as a linear combination of subspace basis vectors  $|\psi_k\rangle = \hat{U}(\Delta_t)^k |\phi_0\rangle$ , where  $\hat{U}$  is an unitary operator approximating the time evolution  $e^{-i\Delta_t H}$  with a Trotter expansion (for ease of notation we absorb  $\hbar$  into our definition of time). Here  $k \in [-n_l, n_l]$ , where  $n_l$  is an integer that sets the size of the basis used to expand the Krylov vectors [24]. One then needs to evaluate on the quantum computer the overlap and Hamiltonian matrix elements for these basis vectors, given by

$$S_{ij} = \langle \phi_0 | \hat{U}(\Delta_t)^{-i} \hat{U}(\Delta_t)^j | \phi_0 \rangle, \qquad (6)$$

$$H_{ij} = \langle \phi_0 | \hat{U}(\Delta_t)^{-i} \hat{H} \hat{U}(\Delta_t)^j | \phi_0 \rangle, \qquad (7)$$

respectively. These can be obtained on a quantum computer with different methods, such as for example the Hadamard test [48]. To perform the Trotter expansion we use the scheme in Ref. [24], where the time evolution of the quadratic part of the Hamiltonian is performed exactly. The evaluation of these matrix elements

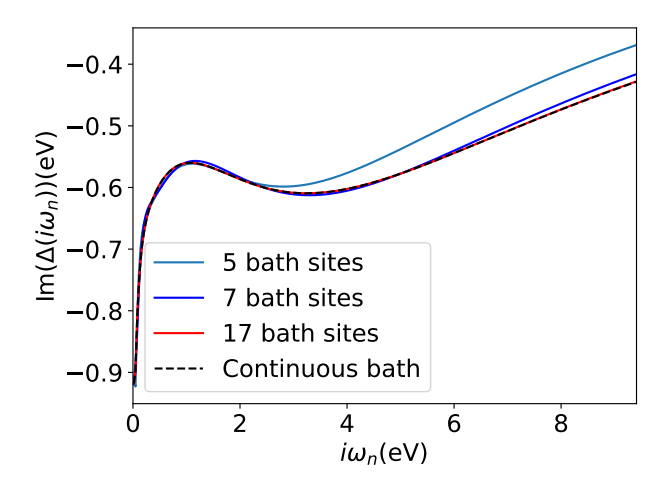


Figure 2. Comparison between the target continuous bath hybridization function (black dashed line) and the hybridization function for a discretized bath with increasing number of bath sites, on the imaginary axis  $(\omega_n = (2n+1)\pi/\beta_f)$ .

on the quantum computer is schematically illustrated in the third box in Fig. 1. We note that one may greatly reduce the number of matrix elements that needs to be computed by exploiting the fact that  $S_{ij}$  is a Toeplitz matrix, where the elements only depend on i-j, and that, if a small enough Trotter step is used, then also  $H_{ij}$  becomes approximately a Toeplitz matrix (see Appendix B for details).

These S and H matrices obtained on a quantum computer are then used on a classical computer to perform the orthogonalized Krylov basis construction [24], and with it to obtain the GF and the DOS. This is schematically illustrated in the last panel in Fig. 1.

We demonstrate our algorithm on the prototypical strongly correlated metal with perosvskite structure  $SrVO_3$  [49, 50], where a non-perturbative method such as DMFT is required to obtain the correct renormalization of the quasi-particle bands. We first compute the ground state using density functional theory within the local density approximation with the Questaal code [51]. Then, the DMFT subspace is constructed via local projection onto the three V  $t_{2q}$  orbitals. The continuous bath is discretized by fitting the hybridization function,  $\Delta$ , with a finite number of bath orbitals on the Matsubara axis for a fictitious inverse temperature of  $\beta_f=200 \text{ eV}^{-1}$ . The finite  $\beta_f$  broadens sharp peaks in the hybridization, so that it can be computed with a finite grid on the imaginary axis. In Fig. 2 we plot the obtained hybridization function of the first DMFT iteration with 5, 7 and 17 bath orbitals on the Matsubara axis, and compare it to the target continuous bath hybridization. There is a significant discrepancy between the five bath orbitals results and the continuous bath solution, while for seven bath orbitals the agreement is rather good, until it becomes effectively exact for 17 bath sites.

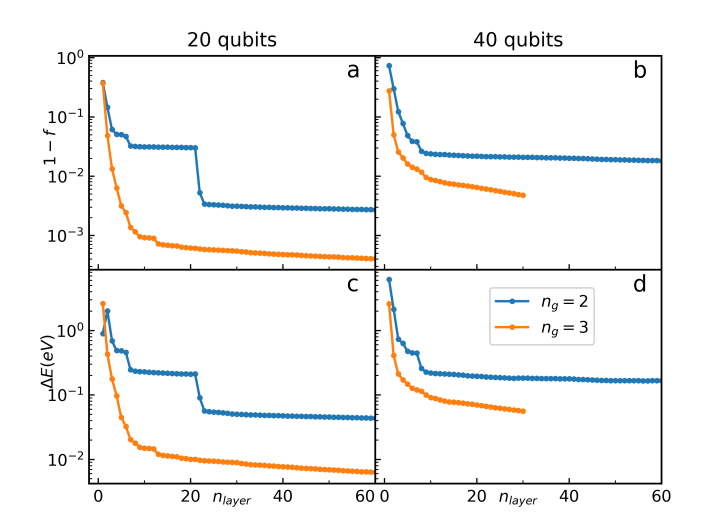


Figure 3. Deviation from unity of the overlap (upper panel), and energy difference (lower panel) of the optimized quantum circuit with respect to the number of staircase layers in the circuit for the SrVO<sub>3</sub> GS with 3 impurity sites, for 7 bath orbitals (a-b), and for 17 bath orbitals (c-d).

We therefore perform the computation for the GS for the three impurity sites coupled to 7 and 17 bath sites, requiring 20 and 40 qubits in total, respectively, when using the Jordan-Wigner transform and two spins per site. We make use of a set of orbitals for the bath that make the hopping matrix (containing the hopping matrices for the impurity,  $\epsilon_{ij}$ , and bath,  $\epsilon_{ij}^d$ , orbitals and the hybridization matrix,  $V_{ij}$ ) block tridiagonal, where each block has a dimension of  $n_{\rm imp}$ . We perform a DMRG calculation, as implemented in ITensor [29, 30], to obtain the GS MPS wave function,  $|\psi_{\rm MPS}\rangle$ , and GS energy,  $E_{\rm GS}$ . We use 30 DMRG sweeps and a truncation error cutoff of  $10^{-7}$ . For the 20 qubits system the maximum bond dimension reached during the optimization is 48, while for the 40 qubit system a bond dimension of 169 is required.

We then set up the quantum circuits to obtain  $|\psi_{QC}\rangle$ by performing the maximization of the overlap in Eq. 4 for different  $n_{\rm g}$  and  $n_{\rm layer}$ . Figure 3 presents the convergence of the quantum circuit to the MPS state with the number of layers. Figure 3a (c) presents the convergence in terms of 1-f for the 20 (40) qubit calculation, and Fig. 3b (d) shows the corresponding energy difference,  $\Delta E$ , of the optimized quantum circuit as a function of  $n_{\text{layer}}$ , for  $n_{\text{g}}$  equal to 2 and 3. We find that for  $n_{\rm g}=3$  the energy and overlap converge systematically to progressively better accuracy, while the  $n_g = 2$ circuits exhibit plateaus in the convergence followed by sudden jumps. The same convergence behavior in terms of corresponding CNOT gates obtained using the optimized quantum Shannon decomposition [35] is presented in Appendix A (Fig. 5). In general for a given  $n_{\text{layer}}$ , the circuit depth, and with it the total number of CNOT gates, for  $n_{\rm g}=3$  is significantly larger than for  $n_{\rm g}=2$ .

The overlap has to be relatively large to obtain an energy difference of less than 10 meV. In the 40 qubit case we can obtain a overlap of  $\approx 98\%$  with 2-qubit gates before it reaches a plateau, and  $\Delta E=0.2$  eV. The results show that for both 20 and 40 qubits we obtain the quantum circuit representation of the GS with increasing overlap as we increase the circuit depth. If the number of CNOT gates is not a major limitation of the device, which may occur in the fault-tolerant era, increasing  $n_{\rm g}$  helps to achieve high overlap. However, if minimizing the number of CNOT gates is important, 2-qubit gates can usually achieve better accuracy with smaller numbers of CNOT gates.

Having obtained the quantum circuit for the GS wave function using the TN classical computing approach above, we can execute the circuit on a quantum computing emulator. With this  $|GS\rangle = |\psi_{\rm QC}\rangle$  we then evaluate the matrix elements in Eqs. 6 and 7 by performing the Trotter time evolution, and with them obtain the GF (see schematic 1). We use the Qulacs state vector emulator [52] to perform these simulations. Since the computing resources required in these state vector emulations are much higher than for our MPS based GS computations, we can only simulate the 20 qubits system, while the 40 qubits system is beyond what we can reach with our available resources. We use a Trotter step of  $\Delta_t = 0.1 \; {\rm eV}^{-1}$  and  $n_l = 300$  for the basis used in the QSEG algorithm.

We systematically evaluate the quality of the obtained GF for different levels of overlap  $f = |\langle \psi_{\text{MPS}} | \psi_{\text{QC}} \rangle|$ . To this aim we compute the exact reference GF using an exact diagonalization technique [45, 53]. In Figs. 4a-d we compare the local DOS (DOS( $\omega$ ) =  $-\frac{1}{\pi} \text{Im} G(\omega + i\delta)$ , where here we use  $\delta = 0.1 \text{ eV}$ ) obtained using the compiled quantum circuit representations of the MPS GS with increasing overlap. We find that only for the highest achieved overlap the DOS is in approximate agreement with the exact reference DOS. While this shows that the algorithm works, it may also suggest that very high fidelities, and hence accurate GS energies, are required for the quantum circuit representation of the GS wave function.

To obtain an accurate GF also for lower values of the overlap we note that a significant part of the difference from the exact DOS is caused by shifts in the peaks. One reason for such shifts is that the GS energy computed with the quantum circuit,  $E_{\rm QC} = \langle \psi_{\rm QC} | \hat{H} | \psi_{\rm QC} \rangle$ , differs from the exact  $E_{\rm GS}$ , as shown in Fig. 3. To improve the GF obtained with our quantum algorithm we therefore take advantage of the fact that we have access to the exact MPS GS energy  $E_{\rm GS}$  independently of its quantum circuit representation, and use this energy  $E_{\rm GS}$  in Eqs. 2 and 3 for the computation of the GFs. The results when

using this approach are shown in Figs. 4e-h. One can see that with this method the DOS converges to the exact DOS already at much lower values of the overlap of about 0.95. This is an important advantage of our scheme: we do not need to have a perfect match between the exact GS and the compiled quantum circuit, because the exact GS energy is obtained with excellent numerical precision on a classical computer. We expect that also for the 40 qubit calculation, where we obtain an overlap of 98% when using 2-qubit gates and 99% with 3-qubit gates (see Fig. 3), one would be able to obtain an accurate GF if the time-evolution could be executed, either on an emulator with larger classical computing resources, or directly on a quantum computer.

In conclusion, in this article we have proposed an Anderson impurity solver using classical and quantum computing resources. The GS is first determined with classical TN methods, and then a quantum circuit representing this GS is constructed on the classical computer. This circuit can be executed on a quantum computer, and subsequently time evolution of the state can be performed to obtain the Hamiltonian and overlap matrix elements within a quantum subspace expansion approach, and with these the GF is obtained. Combining the strengths of the classical and quantum methods allows us to obtain the GF of an impurity model for the real material SrVO<sub>3</sub>, represented on 20 qubits on an emulator. For 40 qubits we obtain an overlap with the GS that could allow the construction of the GF if either larger classical computing resources would be available for the time evolution quantum emulation, or if the time evolution was executed directly on a quantum computer. To further improve the scalability of the classical tensor network computation, this method can be extended to more general tree tensor networks or fork tensor networks, which have shown success for treating multi-orbital impurity models [8, 9].

## Acknowledgments

The authors acknowledge the support of the UK government department for Business, Energy and Industrial Strategy through the UK National Quantum Technologies Programme. FJ acknowledges support through an Explorers Award from the National Physical Laboratory's Directors' Science and Engineering Fund. EF acknowledges the support of an industrial CASE (iCASE) studentship, funded by the UK Engineering and Physical Sciences Research Council (grant EP/T517665/1), in collaboration with the university of Strathclyde, the National Physical Laboratory, and Quantinuum.

R. P. Feynman, Int. J. Theor. Phys. 21, 467 (1982).

<sup>[2]</sup> S. Lloyd, Science **273**, 1073 (1996).

<sup>[3]</sup> A. Georges, G. Kotliar, W. Krauth, and M. J. Rozenberg, Rev. Mod. Phys. 68, 13 (1996).

<sup>[4]</sup> G. Kotliar, S. Y. Savrasov, K. Haule, V. S. Oudovenko, O. Parcollet, and C. A. Marianetti, Rev. Mod. Phys. 78, 865 (2006).

<sup>[5]</sup> D. Vollhardt, Ann. Phys. (Berlin) **524**, 1 (2012).

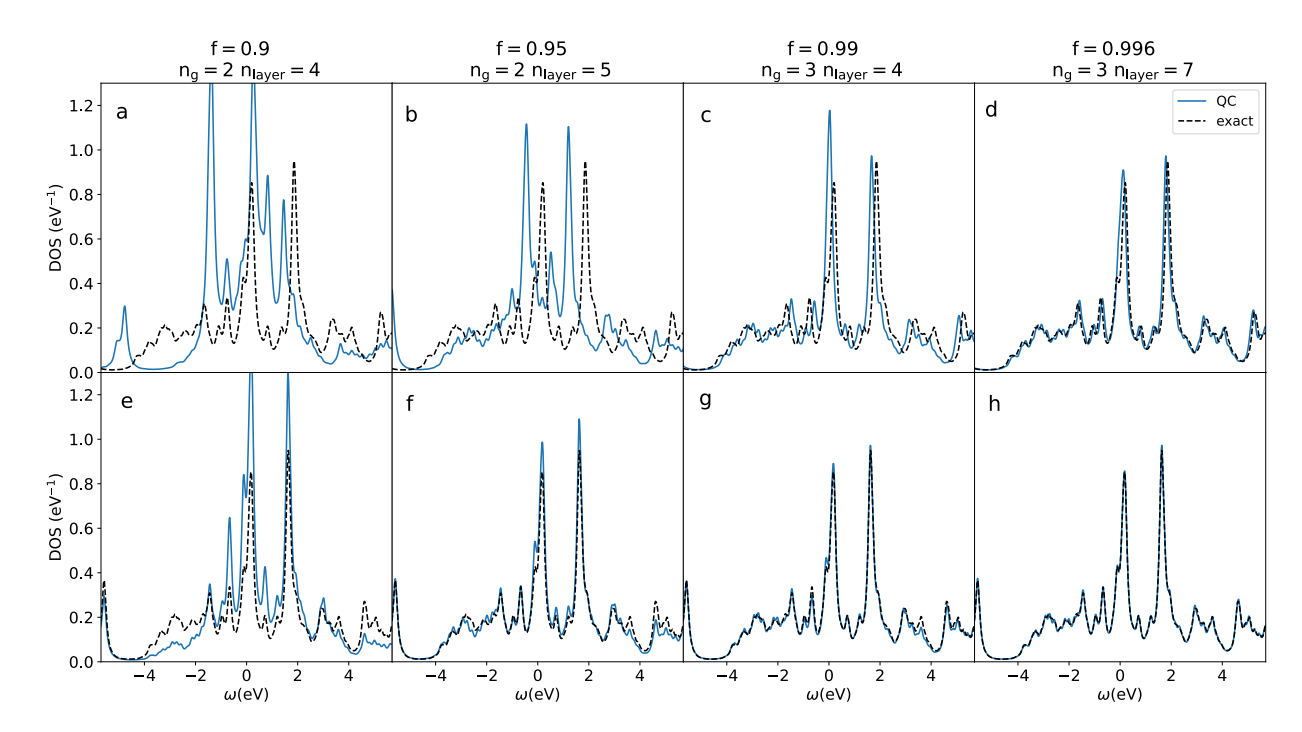


Figure 4. The local DOS of the first DMFT iteration for SrVO<sub>3</sub> computed with the MPS+QSEG algorithm for  $n_l = 300$  and  $\Delta_t = 0.1 \text{ eV}^{-1}$ . Here we show the DOS of the  $t_{2g}$  xy orbital (the two other  $t_{2g}$  orbitals have very similar accuracy). The upper panels (a-d) show the GF computed with the approximate GS energy obtained on the quantum circuit  $(E_{QS} = \langle \psi_{QC} | \hat{H} | \psi_{QC} \rangle)$ , and the lower panels (e-h) show the results for the accurate MPS GS energy  $(E_{GS} = \langle \psi_{MPS} | \hat{H} | \psi_{MPS} \rangle)$ . In each panel we compare the DOS obtained using the quantum circuit representation of the GS (blue solid lines) with the DOS obtained using an exact diagonalization technique (black dashed lines). The GS overlap f for each DOS is given above the panels, as well as the used values of  $n_g$  and  $n_{\text{layer}}$  to obtain this overlap.

- [6] A. Paul and T. Birol, Annu. Rev. Mater. Res. 49, 31 (2019).
- [7] H. Aoki, N. Tsuji, M. Eckstein, M. Kollar, T. Oka, and P. Werner, Rev. Mod. Phys. 86, 779 (2014).
- [8] D. Bauernfeind, M. Zingl, R. Triebl, M. Aichhorn, and H. G. Evertz, Phys. Rev. X 7, 031013 (2017).
- [9] X. Cao, Y. Lu, P. Hansmann, and M. W. Haverkort, Phys. Rev. B 104, 115119 (2021).
- [10] F. A. Wolf, A. Go, I. P. McCulloch, A. J. Millis, and U. Schollwöck, Phys. Rev. X 5, 041032 (2015).
- [11] M. Ganahl, P. Thunström, F. Verstraete, K. Held, and H. G. Evertz, Phys. Rev. B 90, 045144 (2014).
- [12] F. A. Wolf, I. P. McCulloch, O. Parcollet, and U. Schollwöck, Phys. Rev. B 90, 115124 (2014).
- [13] F. A. Wolf, J. A. Justiniano, I. P. McCulloch, and U. Schollwöck, Phys. Rev. B 91, 115144 (2015).
- [14] M. Schüler, C. Renk, and T. O. Wehling, Phys. Rev. B 91, 235142 (2015).
- [15] R. Bulla, T. A. Costi, and T. Pruschke, Rev. Mod. Phys. 80, 395 (2008).
- [16] K. M. Stadler, Z. P. Yin, J. von Delft, G. Kotliar, and A. Weichselbaum, Phys. Rev. Lett. 115, 136401 (2015).
- [17] P. Werner, A. Comanac, L. de' Medici, M. Troyer, and A. J. Millis, Phys. Rev. Lett. 97, 076405 (2006).
- [18] B. Bauer, D. Wecker, A. J. Millis, M. B. Hastings, and M. Troyer, Phys. Rev. X 6, 031045 (2016).
- [19] T. Keen, B. Peng, K. Kowalski, P. Lougovski, and S. Johnston, Quantum 6, 675 (2022).

- [20] D. Gobert, C. Kollath, U. Schollwöck, and G. Schütz, Phys. Rev. E 71, 036102 (2005).
- [21] J. Eisert and T. J. Osborne, Phys. Rev. Lett. 97, 150404 (2006).
- [22] R. Peters, Phys. Rev. B 84, 075139 (2011).
- [23] P. Wissgott, J. Kuneš, A. Toschi, and K. Held, Phys. Rev. B 85, 205133 (2012).
- [24] F. Jamet, A. Agarwal, and I. Rungger, Quantum subspace expansion algorithm for green's functions (2022), arXiv:2205.00094.
- [25] S. R. White, Phys. Rev. Lett. 69, 2863 (1992).
- [26] S. R. White, Phys. Rev. B 48, 10345 (1993).
- [27] U. Schollwöck, Rev. Mod. Phys. **77**, 259 (2005).
- [28] U. Schollwöck, Ann. Phys. **326**, 96 (2011).
- [29] M. Fishman, S. R. White, and E. M. Stoudenmire, Sci-Post Phys. Codebases, 4 (2022).
- [30] M. Fishman, S. R. White, and E. M. Stoudenmire, Sci-Post Phys. Codebases , 4 (2022).
- [31] M. B. Dov, D. Shnaiderov, A. Makmal, and E. G. D. Torre, Approximate encoding of quantum states using shallow circuits (2022), arXiv:2207.00028.
- [32] M. S. Rudolph, J. Chen, J. Miller, A. Acharya, and A. Perdomo-Ortiz, Decomposition of matrix product states into shallow quantum circuits (2022), arXiv:2209.00595.
- [33] S.-H. Lin, R. Dilip, A. G. Green, A. Smith, and F. Poll-mann, PRX Quantum 2, 010342 (2021).
- [34] R. Dilip, Y.-J. Liu, A. Smith, and F. Pollmann, Phys. Rev. Res. 4, 043007 (2022).

- [35] V. Shende, S. Bullock, and I. Markov, IEEE Transactions on Computer-Aided Design of Integrated Circuits and Systems 25, 1000 (2006).
- [36] S.-J. Ran, Phys. Rev. A **101**, 032310 (2020).
- [37] J. Dborin, F. Barratt, V. Wimalaweera, L. Wright, and A. G. Green, Quantum Sci. Technol. 7, 035014 (2022).
- [38] T. Shirakawa, H. Ueda, and S. Yunoki, Automatic quantum circuit encoding of a given arbitrary quantum state (2021), arXiv:2112.14524.
- [39] R. Babbush, C. Gidney, D. W. Berry, N. Wiebe, J. Mc-Clean, A. Paler, A. Fowler, and H. Neven, Phys. Rev. X 8, 041015 (2018).
- [40] D. W. Berry, M. Kieferová, A. Scherer, Y. R. Sanders, G. H. Low, N. Wiebe, C. Gidney, and R. Babbush, npj Quantum Inf. 4 (2018).
- [41] B. Jaderberg, A. Agarwal, K. Leonhardt, M. Kiffner, and D. Jaksch, Quantum Sci. Technol. 5, 034015 (2020).
- [42] S. Endo, I. Kurata, and Y. O. Nakagawa, Phys. Rev. Research 2, 033281 (2020).
- [43] T. Keen, T. Maier, S. Johnston, and P. Lougovski, Quantum Sci. Technol. 5, 035001 (2020).
- [44] I. Rungger, N. Fitzpatrick, H. Chen, C. H. Alderete, H. Apel, A. Cowtan, A. Patterson, D. Munoz Ramo, Y. Zhu, N. H. Nguyen, E. Grant, S. Chretien, L. Wossnig, N. M. Linke, and R. Duncan, Dynamical mean field theory algorithm and experiment on quantum computers (2019), arXiv:1910.04735.
- [45] C. Lupo, F. Jamet, W. H. T. Tse, I. Rungger, and C. Weber, Nat. Comput. Sci 1, 502 (2021).
- [46] P. Besserve and T. Ayral, Phys. Rev. B 105, 115108 (2022).
- [47] F. Jamet, A. Agarwal, C. Lupo, D. E. Browne, C. Weber, and I. Rungger, Krylov variational quantum algorithm for first principles materials simulations (2021), arXiv:2105.13298.
- [48] M.-A. Filip, D. M. Ramo, and N. Fitzpatrick, Variational phase estimation with variational fast forwarding (2022), arXiv:2211.16097.
- [49] I. A. Nekrasov, K. Held, G. Keller, D. E. Kondakov, T. Pruschke, M. Kollar, O. K. Andersen, V. I. Anisimov, and D. Vollhardt, Phys. Rev. B 73, 155112 (2006).
- [50] K. Haule and T. Birol, Phys. Rev. Lett. 115, 256402 (2015).
- [51] D. Pashov, S. Acharya, W. R. Lambrecht, J. Jackson, K. D. Belashchenko, A. Chantis, F. Jamet, and M. van Schilfgaarde, Comput. Phys. Commun. 249, 107065 (2020).
- [52] Y. Suzuki, Y. Kawase, Y. Masumura, Y. Hiraga, M. Nakadai, J. Chen, K. M. Nakanishi, K. Mitarai, R. Imai, S. Tamiya, T. Yamamoto, T. Yan, T. Kawakubo, Y. O. Nakagawa, Y. Ibe, Y. Zhang, H. Yamashita, H. Yoshimura, A. Hayashi, and K. Fujii, Quantum 5, 559 (2021).
- [53] C. Weber, A. Amaricci, M. Capone, and P. B. Littlewood, Phys. Rev. B 86, 115136 (2012).

## Appendix A: CNOT count of $n_g$ -qubit Gates

An arbitrary  $n_{\rm g}$ -qubit unitary operator can be implemented on a quantum computer using one-qubit gates  $(R_x,\ R_y,\ R_z)$  and CNOT gates. Table I provides the number of CNOT gates required to implement one general  $n_{\rm g}$ -qubit gate using the optimized quantum Shannon decomposition, which is given by  $N_{\rm CNOT}=\frac{23}{48}4^{n_g}-\frac{3}{2}2^{n_g}+\frac{4}{3}$  [35], for  $n_{\rm g}$  up to 5.

Number of qubits	CNOT gate count
2	3
3	20
4	100
5	444

Table I. CNOT count of a n<sub>g</sub>-qubit gate using the optimized quantum Shannon decomposition. [35]

Figure 5a(c) presents the difference from unity of the overlap f for the 20 (40) qubit calculation, and Fig. 5b(d) shows the corresponding energy difference,  $\Delta E$ , of the optimized quantum circuit as shown in Fig. 3 of the main text, but now as a function of the total number of CNOT gates, for  $n_g$  equal to 2 and 3. While the choice of using 3-qubit unitaries does give rise to smoother convergence of the resultant circuit, here we observe that, for the 20 qubit case, this choice does not dramatically reduce the number of CNOT gates required to obtain solutions with overlaps of f < 0.99. For the 40 qubit case, the use of 2-qubit gates leads to significantly better overlaps for low CNOT counts, however, we find that the use of 3-qubit gates leads to reductions in the CNOT count for overlaps of f > 0.98. In both the 20 and 40 qubit cases, the number of CNOT gates required by this decomposition scheme is considerably smaller than would be required if a direct mapping of the MPS into a single layer of  $n_q =$  $\lceil \log_2(\chi) \rceil + 1$  qubit unitaries were performed. Performing such a mapping the 20 qubit case would require  $\sim 6 \times 10^4$ CNOT gates, where as the 40 qubit case would require  $\sim 2 \times 10^6$  CNOT gate.

Some of the unitaries in the staircase ansatz can be performed in parallel which reduces the depth - in terms of non-parallel CNOT gates - of the circuit to  $((n_l-1)n_g+(n_q-n_g+1))N_{CNOT}(n_g)$ , with  $n_l$  the number of layers and  $n_{\rm q}$  is the total number of qubits. Figure 6 presents the same data as shown in Fig. 5, namely the difference from unity of the overlap f for the 20 (40) qubit calculation, and Fig. 6b(d) shows the corresponding energy difference,  $\Delta E$ , but now as a function of the number of non-parallel CNOT gates. In terms of the depth the circuit of 2 qubit unitaries is more efficient in reaching an infidelity of  $\approx 2 \times 10^{-2}$  for 40 qubits, but it is unclear whether it could gain a much improved accuracy with a much higher depth. The ansatz of 3 qubit unitaries, on the other hand, can reach a higher fidelity with our available classical computational resources, but

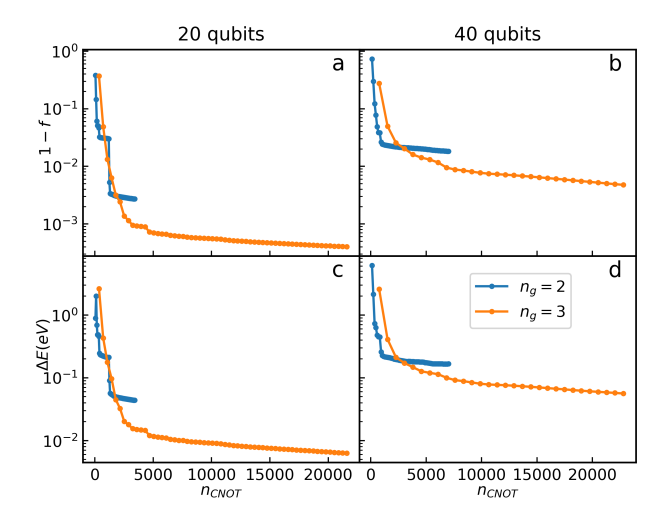


Figure 5. Deviation from unity of the overlap (upper panel), and energy difference (lower panel) of the optimized quantum circuit with respect to the total number of CNOT gates in the circuit for the SrVO<sub>3</sub> GS with 3 impurity sites, for 7 bath orbitals (a-b), and for 17 bath orbitals (c-d).

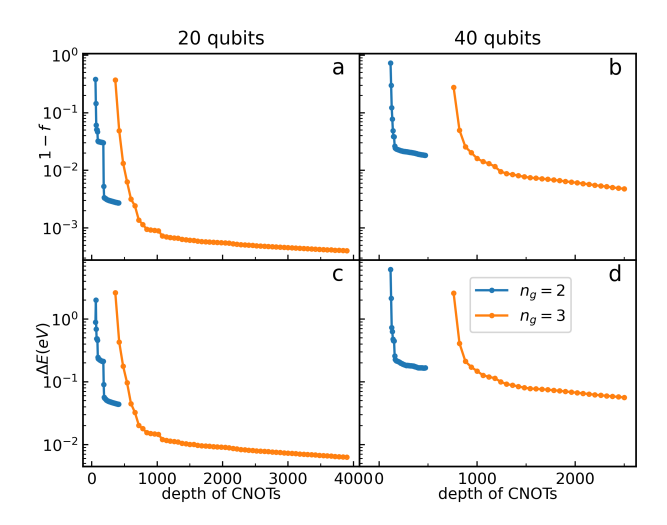


Figure 6. Same data as plotted in Fig. 5, where the horizontal axis now is the circuit depth measured as the number of non-parallel CNOT gates in the circuit.

has a much higher depth for even one layer of gates.

## Appendix B: Reducing the number of matrix elements that needs to be computed

For each matrix  $S_{ij}$  and  $H_{ij}$  (Eqs. 6 and 7 in the main text) there are  $(2n_l+1)^2$  matrix elements. Both matrices are symmetric, reducing the number of independent elements to  $\frac{(2n_l+1)(2n_l+2)}{2}$ . Moreover,  $S_{ij}$  is a Toeplitz matrix (its elements only depend on i-j), further significantly reducing the number of its independent elements to only  $2n_l+1$ . If the time evolution operator  $\hat{U}(\Delta_t)$  is executed exactly, one has  $H_{ij} = \langle \phi_0 | \hat{H} \hat{U}(\Delta_t)^{j-i} | \phi_0 \rangle$ ,

since in this case  $\hat{H}$  commutes with  $\hat{U}(\Delta_t) = e^{-i\Delta_t H}$ , making  $H_{ij}$  a Toeplitz matrix as well.

In practice, however,  $\hat{U}(\Delta_t)$  is executed approximately, hence  $\hat{H}$  only approximately commutes with  $\hat{U}(\Delta_t)$ . More precisely, in this work the time evolution operator is approximated by the Trotter expansion  $\hat{U}(\Delta_t) \approx e^{-i\hat{H}_{\rm int}\Delta_t/2}e^{-i\hat{H}_0\Delta_t}e^{-i\hat{H}_{\rm int}\Delta_t/2}$ , where the error scales as  $\mathcal{O}(\Delta_t^3)$ . Here we have introduced

$$H_{0} = \sum_{ij}^{n_{\text{imp}}} \sum_{\sigma} \epsilon_{ij} \hat{c}_{i\sigma}^{\dagger} \hat{c}_{j\sigma} + \sum_{\sigma} \sum_{ij}^{n_{b}} \epsilon_{ij}^{d} \hat{d}_{i\sigma}^{\dagger} \hat{d}_{j\sigma}$$
$$+ \sum_{i}^{n_{\text{imp}}} \sum_{j}^{n_{b}} \sum_{\sigma} V_{ij} (\hat{c}_{i\sigma}^{\dagger} \hat{d}_{j\sigma} + \hat{d}_{j\sigma}^{\dagger} \hat{c}_{i\sigma}), \qquad (B1)$$

$$H_{\text{int}} = \sum_{ijkl}^{n_{\text{imp}}} \sum_{\sigma\sigma'} U_{ijlk} \hat{c}_{i\sigma}^{\dagger} \hat{c}_{j\sigma'}^{\dagger} \hat{c}_{k\sigma'} \hat{c}_{l\sigma}.$$
 (B2)

Therefore, as  $\Delta_t$  decreases, the error introduced by performing the commutation  $H_{ij} = \langle \phi_0 | \hat{U}(\Delta_t)^{-i} \hat{H} \hat{U}(\Delta_t)^j | \phi_0 \rangle \approx \langle \phi_0 | \hat{H} \hat{U}(\Delta_t)^{j-i} | \phi_0 \rangle$  also decreases, until  $H_{ij}$  becomes a Toeplitz matrix to a good approximation. However, decreasing  $\Delta_t$  also increases the depth of the circuit required to reach a given total evolution time. Therefore it needs to be verified whether performing the commutation leads to a reasonable error for practical values of  $\Delta_t$ .

We test the resulting accuracy of the GF for our SrVO<sub>3</sub> AIM system when using the approximation  $H_{ij} \approx \langle \phi_0 | \hat{H} \hat{U}(\Delta_t)^{j-i} | \phi_0 \rangle$  for two different values of  $\Delta_t$ , namely  $\Delta_t = 0.05 \, \text{eV}^{-1}$  and  $\Delta_t = 0.1 \, \text{eV}^{-1}$ . We keep the number of basis states in the subspace expansion equal to  $n_l = 300$  for both cases, so that all circuits have the same depth. The other parameters are the same as those used for the DOS plot in Fig. 4h. The upper panels of Fig. 7 show the DOS obtained using  $H_{ij}$  as defined in Eq. 7, while the DOS shown in the bottom panels is obtained using the approximation  $H_{ij} \approx \langle \phi_0 | \hat{H} \hat{U}(\Delta_t)^{j-i} | \phi_0 \rangle$ . For  $\Delta_t = 0.1 \text{ eV}^{-1}$ , which is the value also used in the calculation in the main text for Fig. 4h, the use of the approximated  $H_{ij}$  gives a DOS that is quite close to the one obtained by exact diagonalization (dashed black line), although it is notably different in some energy ranges, in particular at the Fermi energy,  $\omega = 0$ . For  $\Delta_t = 0.05$  $eV^{-1}$  the approximated DOS is in very good agreement with the exact DOS. These results confirm that the approximated relation  $H_{ij} \approx \langle \phi_0 | \hat{H} \hat{U}(\Delta_t)^{j-i} | \phi_0 \rangle$  can be applicable in practical calculations provided that  $\Delta_t$  is small enough, in which case the number of matrix elements to be computed is significantly reduced by taking advantage of the Toeplitz form of the matrix. Whether for a general system it is feasible to reach the small  $\Delta_t$ required depends on the details of the system, the characteristics of the quantum device, and the construction of the time evolution circuit, and must be assessed on a case-by-case basis.

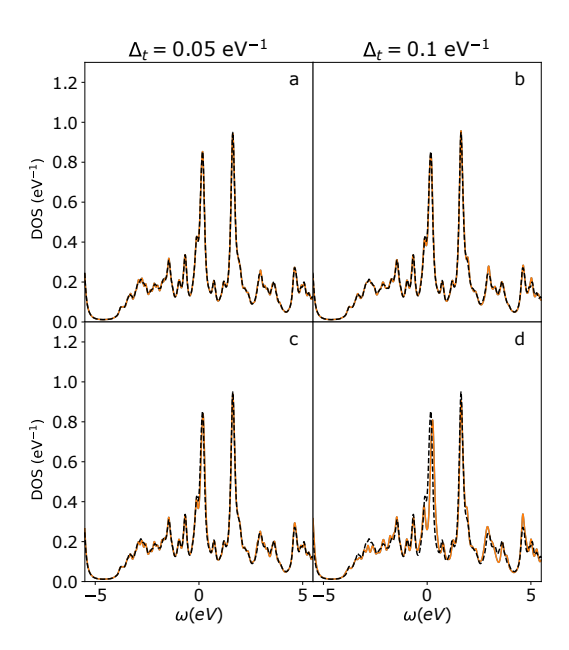


Figure 7. The DOS of the impurity model calculated using MPS+QSEG (orange curves) for  $\Delta_t = 0.05 \; \mathrm{eV}^{-1}$  (left panels) and  $\Delta_t = 0.1 \; \mathrm{eV}^{-1}$  (right panels), compared with the exact diagonalization result (dashed black line). The upper panels show the DOS obtained using  $H_{ij}$  as defined in Eq. 7, while the DOS shown in the bottom panels is obtained using the approximation  $H_{ij} \approx \langle \phi_0 | \hat{H} \hat{U} (\Delta_t)^{j-i} | \phi_0 \rangle$ .